

Supporting information for

Field Evidence of Fe-Mediated Photochemical Degradation of Oxalate and Subsequent Sulfate Formation Observed by Single Particle Mass Spectrometry

Yang Zhou^{1,2*}, Yanjing Zhang¹, Stephen M. Griffith^{3,4}, Guanru Wu¹, Lei Li⁵, Yunhui Zhao¹, Mei Li⁵, Zhen Zhou⁵, Jian Zhen Yu^{2, 3, 6,*}

¹ Physical Oceanography Laboratory/CIMST, Ocean University of China and Qingdao National Laboratory for Marine Science and Technology, Qingdao 266100, China

² Institute of Environment, Hong Kong University of Science and Technology, Clear Water Bay, Kowloon, Hong Kong, China

³ Department of Chemistry, Hong Kong University of Science and Technology, Clear Water Bay, Kowloon, Hong Kong, China

⁴ Department of Atmospheric Sciences, National Central University, Taoyuan, Taiwan

⁵ Institute of Atmospheric Environment Safety and Pollution Control, Jinan University, Guangdong 510632, China

⁶ Division of Environment, The Hong Kong University of Science and Technology, Clear Water Bay, Kowloon, Hong Kong, China.

* Corresponding author: Yang Zhou (yangzhou@ouc.edu.cn) Jian Zhen Yu (jian.yu@ust.hk),

This file includes

S1: Introduction of SPAMS (Figure S1)

S2: Statistics of oxalate-containing particles and comparison between MARGA and SPAMS (Table S1 to S2, Figure S2)

S3: Discussion on the 14 classified groups of oxalate particles and possible sources (Table S3, Figure S3 to S4)

S4: Diurnal variations of oxalate and classified or unclassified oxalate and oxalate-HM information (Figure S5-S12)

S5: Temporal variations of oxalate-Fe complexes (Figure S13)

S6: Discussion on the minimizing the uncertainty of semi-quantification analysis by SPAMS (Figure S14-15)

S1. Introduction of SPAMS (Figure S1)

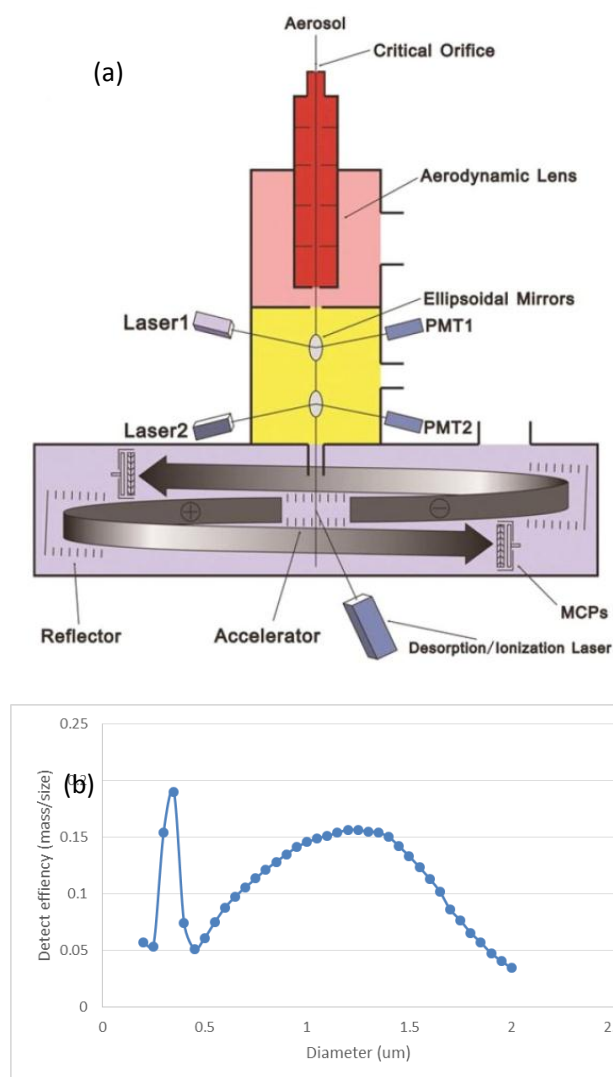


Figure S1. a) Schematic diagram of the single particle aerosol mass spectrometer (SPAMS, from Hexin Analytical Instrument Co.) and b) the average hit rate of the instrument during this study.

Individual particles with diameters from 0.2~2.0 μm were chemically characterized by a single particle aerosol mass spectrometer (SPAMS)¹. Particles are introduced from the ambient air into the vacuum system through a $\sim 100 \mu\text{m}$ critical orifice, and then pass through an aerodynamic lens where the particles are accelerated to a size-dependent velocity, due to the pressure difference, and are gradually focused onto the axis of the lens. As the particle beam passes through two 532 nm continuous lasers, photomultiplier tubes (PMTs) associated with each laser record the time of the particle passing, the difference of which is used to calculate the speed. The size of the particle is achieved by knowing the speed and calibrating with a polystyrene latex (PSL) particle of known size. Sized particles are individually ionized in the center of the ion source region by a pulsed 266 nm Nd:YAG laser (1.0 mJ). Both positive and negative ions are then detected and analyzed by a bipolar time-of-flight mass spectrometer. However not all of the particles provide both positive and negative signals; especially the negative ions are usually missing due to suppression by the presence of water.^{2, 3} A Matlab-based toolkit YAADA (<http://www.yaada.org/>)⁴ was used to perform the data searching of particular mass spectral features.

S2: Statistics of oxalate-containing particles and comparison between MARGA and SPAMS (Table S1-S2, Figure S2)

Table S1 The stability constant⁵ and solubility⁶ of oxalate-metal complexes

	Stability constant (T =25°C)		Solubility mg 100 g ⁻¹
	I ^a = 0.10 M	I= 0 M	
K ⁺	- ^b	-0.80	33 000 ^c
Na ⁺	-	-	6300
Mg ²⁺	2.76	3.43	70
Ca ²⁺	-	3	0.67
Cu ²⁺	4.84	6.23	2.53
Zn ²⁺	3.88 ^d	4.87	0.79
Pb ²⁺	4	4.91	0.16
Fe ²⁺	-	3.05 ^e	22
Fe ³⁺	7.53 ^f	7.74 ^g	very soluble
VO ²⁺	-	6.45 ^h	-
Ni ²⁺	-	5.16	1.18
Mn ³⁺	9.98 ⁱ	-	-
Mn ²⁺	3.2	3.95	28
Hg ²⁺	9.66	-	10.7

^a I: Ion strength(M)

^b -: no data

^c solubility in hot water

^d stability constant at 25°C,0.16M

^e stability constant at 25°C,1.0M

^f stability constant at 25°C,0.5M)

^g stability constant at 25°C,3.0M)

^h stability constant at 20°C,1.0M)

ⁱ stability constant at 25°C,1.0M)

Table S2 Particle number and peak area signal statistics of particles measured by Single Particle Aerosol Mass Spectrometry (SPAMS) and bulk measurement mass concentrations

Individual particles ^a	Total Particle	Oxalate	Fe	V	Cu	Zn	Pb
N	2661636	196222	142158	83659	72285	79870	114158
% to total particle	100.0%	7.4%	5.3%	3.1%	2.7%	3.0%	4.3%
	Oxalate	Oxalate_HMs	Oxalate_Fe	Oxalate_V	Oxalate_Cu	Oxalate_Zn	Oxalate_Pb
N	196222	74719	21798	10670	9558	17008	35640
% to oxalate	100.0%	38.1%	11.1%	5.4%	4.9%	8.7%	18.2%
% to oxalate_metals		100.0%	29.2%	14.3%	12.8%	22.8%	47.7%
% to each HMs			15.3%	12.8%	13.2%	21.3%	31.2%
	Oxalate		Fe	V	Cu	Zn	Pb
Peak Area of each species ^b	2.91E+07		9.43E+08	1.96E+08	1.36E+08	1.06E+08	1.66E+08
Compared to the mass concentration ^c		5.7E+07	7.1E+09	1.05E+10	8.98E+09	1.16E+09	4.92E+09
	Oxalate	Oxalate_HMs	Oxalate_Fe	Oxalate_V	Oxalate_Cu	Oxalate_Zn	Oxalate_Pb
Peak Area of m/z 89	2.91E+07	1.25E+07	3.32E+06	1.49E+06	1.72E+06	3.41E+06	6.63E+06
% to m/z 89 in total oxalate	100.0%	42.9%	11.4%	5.1%	5.9%	11.7%	22.8%
% to m/z 89 in oxalate_HMs		100.0%	26.5%	11.9%	13.8%	27.3%	53.0%
Peak Area of HM			9.26E+07	1.87E+07	7.97E+06	2.00E+07	3.41E+07
% to peak area of each metal			24.2%	20.5%	22.8%	37.8%	32.3%
Bulk measurements ($\mu\text{g m}^{-3}$) ^d	PM _{2.5}	Oxalate	Fe	V	Cu	Zn	Pb
Mass concentration	29.04	0.51	0.13	0.019	0.015	0.092	0.034
Stdev	15.32	0.22	0.12	0.015	0.010	0.084	0.023

Note: a Individual particle statistics are based on only those with both negative and positive chemical information; b Peak area statistics are based on the sum of peak area of a target species in the specific particle category; c General comparison for the relative sensitivity of SPAMS; d Average PM_{2.5} and oxalate concentrations are based on the hourly data (total 1260 hours) and metal concentrations are based on filter-based method sampled every 6th day from Feb 04 to Apr 17 (total 12 filters), unit $\mu\text{g m}^{-3}$.

By comparing the traditional filter-based mass concentration and the peak area information obtained by SPAMS, it can be inferred that SPAMS generally has a higher relative sensitivity to metals such as V and Fe than oxalate. In addition, the peak area of metals in the oxalate-HM groups often showed higher contribution to the total metal peak area compared with the contribution by number, e.g. oxalate-Fe particles contributed 24.2% of the Fe peak area, which is higher than the contribution by number (15.3%). These results suggest there was a higher abundance of these metals in the oxalate-HM particles compared with non-oxalate particles.

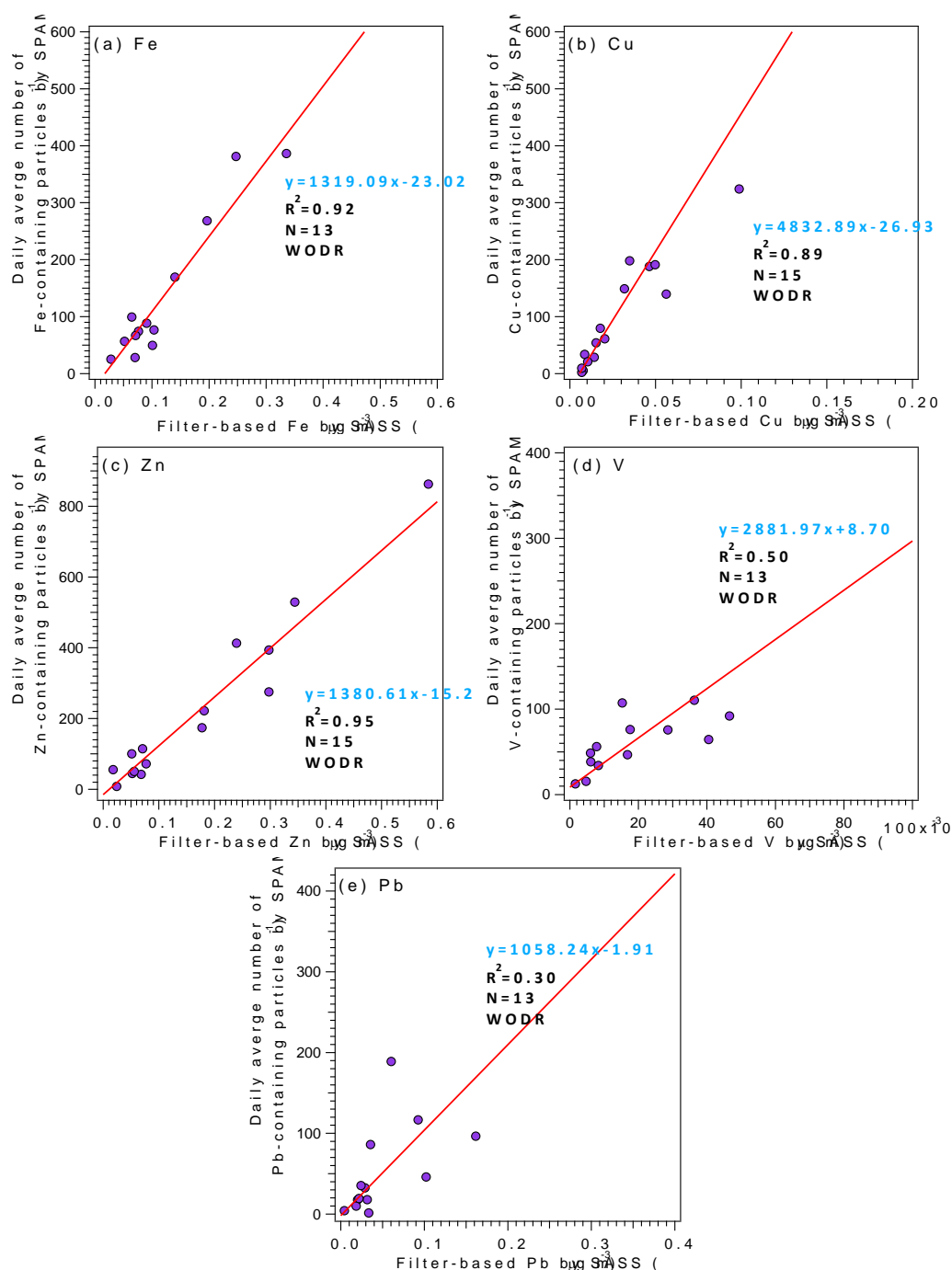


Figure S2 Comparison of metal signal intensity by SPAMS (24h average) with filter-based measurements obtained by Teflon filters using a SASS. The linear regression parameters shown are from WODR (weighted ODR) regression with 10% uncertainty attributed to both methods. Daily metal signal intensity (hourly particle number, # h⁻¹) measured by SPAMS were obtained by averaging 24 hours of unscaled hourly particle number intensity. And these daily average data were compared with bulk filter concentrations measured by X-Ray Fluorescence (XRF). Good correlations were observed for Fe, Cu and Zn (R^2 of 0.92, 0.89 and 0.95 respectively, **Figure S2 a~c**), while moderate correlations were obtained for V and Pb (R^2 of 0.50 and 0.30 respectively, **Figure S2d and e**). Generally, the unscaled SPAMS metal data showed good correlation with bulk measurements (**Figure S2**) suggesting a good detection efficiency of these metals by SPAMS.

S3. Discussion on the classified groups of oxalate particles and possible sources (Table S3, Figure S3-S4)

Table S3 Art-2a classified groups of oxalate particles

Groups	Number	Number Fraction
K_rich	97513	49.7%
K_Na	30320	15.5%
K_ECOC	7493	3.8%
Fe	14283	7.3%
Fe_KNa	6316	3.2%
Pb	9925	5.1%
Zn	3535	1.8%
Cu	2088	1.1%
V	6089	3.1%
SS	3828	2.0%
Dust	3559	1.8%
Dust_K	2536	1.3%
OtherMetal	3540	1.8%
OC_typical	2877	1.5%
Undefined	2320	1.2%
Oxalate	196222	100%

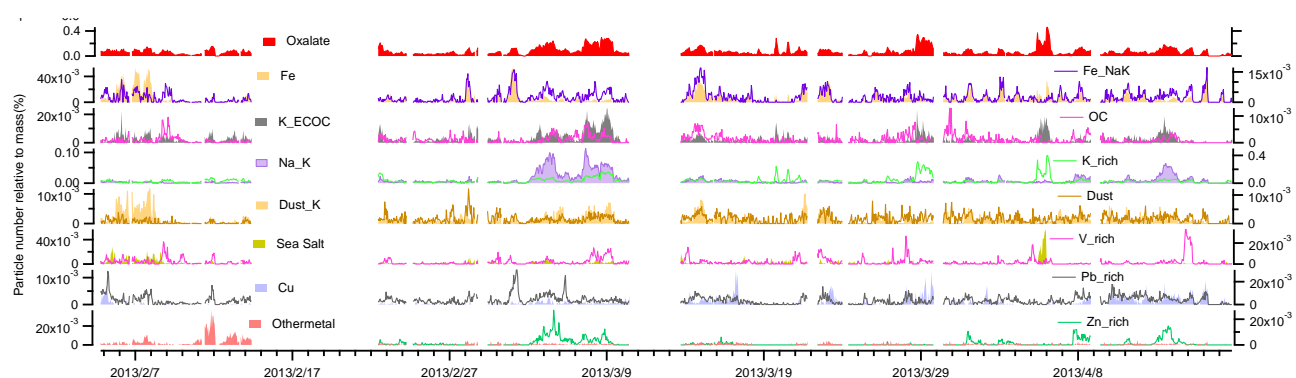


Figure S3 Time series of the major types of oxalate-containing particles, plotted by ratio of oxalate group particle number to mass particle number.

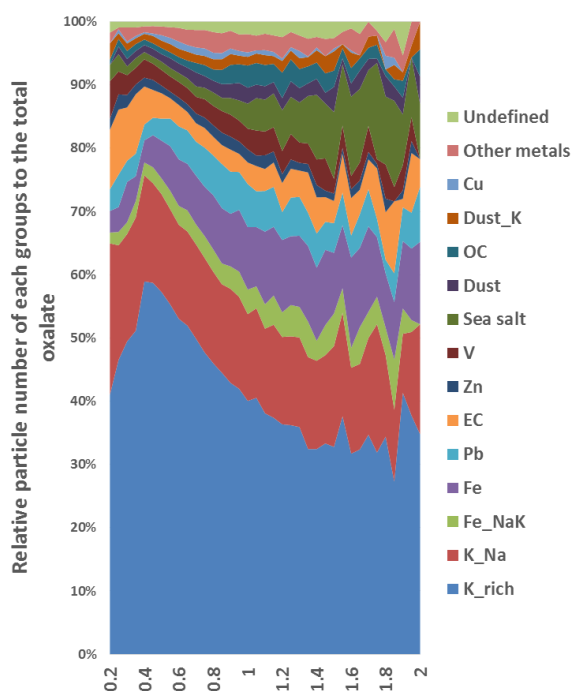


Figure S4 Size-resolved contributions of oxalate particle classes to the total oxalate particles (by number percentage).

S3.1 Oxalate_K related particles

As shown in Figure 1, three classes of oxalate particles, K_{rich}, K_{Na} and K_{ECOC}, were identified with abundant signals of [K]⁺. The dominant sources of oxalate during the campaign were K_{rich} and K_{Na} particles, contributing 49.7% and 15.5% to the total oxalate particles. The K_{rich} and K_{ECOC} particles are typical biomass burning particles, with significant signals from [K]⁺ and levoglucosan (*m/z* at -45, -59 and -73). K_{ECOC} particles showed additional ions from OC (*m/z* 27, 37 and 43) in the positive spectrum and EC fragments (*m/z* ±12*n*) in both positive and negative spectra. However, the K_{Na} group likely comes from a different source, as it had abundant signals from other metals, e.g. Na (*m/z* 23), Fe (*m/z* 54/56), Zn (*m/z* 64/66/67) and Pb (*m/z* 208), and had a different temporal variation compared with K_{rich} and K_{ECOC} particles (Figure S4). As shown in Figures 2 and S4, the most abundant K_{Na} particle period coincided with a Zn_{rich} abundant particle period, suggesting K_{Na} particles are associated with industrial emissions or waste incineration.⁷ In addition, K_{Na} particles were of a relatively larger particle size (Figure S5) and contained more sulfate but less Cl compared with Zn particle types (Figure 2). In other studies, Zn-Pb-Cl particles (Zn_{rich} group in this study) were found to be secondarily formed in the sub-micron mode by a cooling of gas phase zinc and lead chlorides after they are emitted from high temperature combustion processes (e.g. waste incineration, sinter plant)⁸⁻¹⁰. After formation, a fast exchange of Cl with nitrate can occur on these Zn_{rich} particles, thus nitrate could be a dominant negative ion.¹¹ K_{Na} particles may have been more aged since they contained more nitrate and sulfate and less Cl than the Zn_{rich} particles (RPA for Cl is 0.022 vs. 0.065 for K_{Na} and Zn_{rich} particles, respectively in Figure 2). We investigated the spectra and time variation of K_{Na} particles, and found no difference between modes smaller and larger than 1 μm, ruling out the possibility of a coarse dust source for the K_{Na} particles.¹¹

S3.2 Oxalate-heavy metal containing particles

Fe-containing particles, the Fe and Fe_KNa groups, contributed 10.5% to total oxalate particles. The Fe group particles (7.3%), contained abundant m/z 56 signal, were mixed mainly with sulfate and a small portion with nitrate, while Fe_KNa particles (3.2%) showed additional signal from K, Na and Pb and were of a relatively smaller particle size. However, both of these Fe-containing particles followed a very similar temporal variation (Figure S4), so may have originated from the same sources, e.g. industrial emissions.¹¹

V, Pd, Zn and Cu were the four other major metal groups mixed with oxalate, only contributing 3.1%, 5.06%, 1.8% and 1.1% to the total oxalate particle number. It should be noted that a significant number of metal-rich particles detected in the oxalate-containing particles contributed to the submicron fraction (Figure S5), suggesting emission from combustion processes.¹¹ V particles were emitted by marine vessels through residual fuel oil combustion, which often has high sulfur content, thus elevated SO_4^{2-} signals are usually observed mixed with V in fresh ship emission particles.^{12, 13} During transport to the site, particle aging occurs, and can result in the production of NO_3^- on the coating of the V particles since there is abundant NO_x co-emitted during combustion.¹⁴ As mentioned, Zn and PbCl particles usually co-existed in particles, while the other Pb abundant particles were classified into Pb-rich and Cu-rich groups. Pb-rich particles had a dominant m/z 208 positive ion, and small signals from Cu and Fe, while Cu-rich particles showed high intensity of Cu and Pb (Figure 2). As shown in Figure S4, Pb-rich and Cu-rich particles showed similar temporal variation to Fe-containing particles, while much different than the Zn-rich particles. Thus, Pb-rich and Cu-rich particles may be from a similar source as the Fe-containing particles. Although both coal burning and industry emissions are common sources of Fe and Pb,¹⁰ Cu-containing particles have often been observed in aerosols from industries, non-ferrous metal smelters and traffic emissions¹⁵. Thus, oxalate-containing particles with abundant Fe, Pb and Cu could all be from common sources e.g. industrial emissions, metallurgical processes, and non-ferrous metal smelters, while Zn-rich and Na_K particles may be primarily from waste incineration.^{16, 17} From the size resolved contributions of these metals, Fe and Fe_NaK particles showed a relatively high abundance in the coarse mode compared with the other particles, which may be due to iron rich particles being more common at night when the RH is higher and particle water more abundant (See Sec. 3.3 for more details).

S3.3 Other oxalate-containing particles

Sea salt and dust related particles account for 2.0% and 3.1% of the total oxalate particles. Sea salt particles showed minor intensity from Cl^- , but abundant NO_3^- , suggesting the depletion of Cl by nitrate had already occurred. Aged sea salt particles were usually observed by SPAMS for two reasons. Firstly, only small (0.2~2.0 μm) sea salt particles can be detected by SPAMS, and secondly, the depletion of Cl in small size particles is faster than in the coarse mode.¹⁸ Dust particles and dust_K particles are two typical dust related particles. Dust particles showed intense peaks of dust metals, like Al, Ca and some Fe in the positive spectrum and dust_K particles contained high m/z 76 $[SiO_3]^-$ and 60 $[SiO_2]^-$ signals. The dominant $[K]^+$ peaks in the dust_K particles may be attributed to soil dust emitted during biomass burning activities.¹¹

Other metals in this study were mainly firework related metals e.g. Ba Sr and Al, which were only

observed in February during the Spring Festival holiday.

S4: Diurnal variations of oxalate and classified or unclassified oxalate and oxalate-HM information (Figure S5-S12)

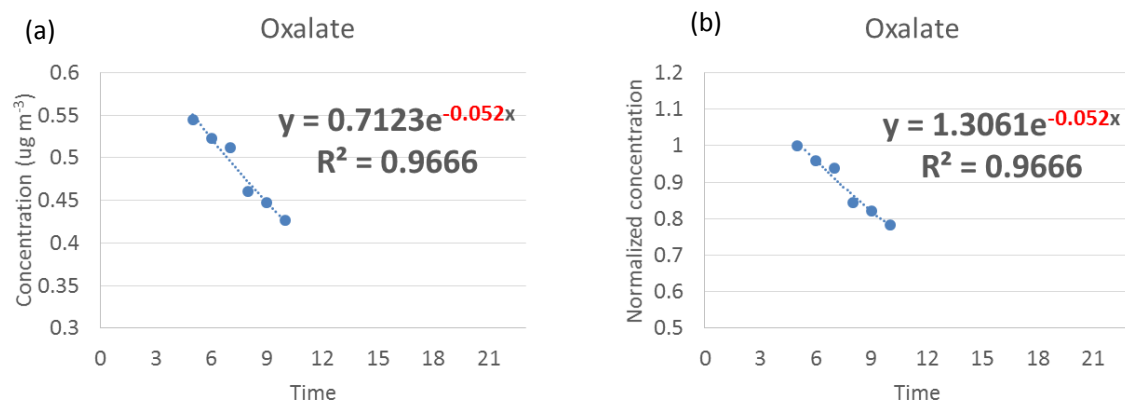


Figure S5 Decay rate of oxalate by a) concentration and b) normalized concentration (the number in red indicates the fitted decay rate based on an exponential curve).

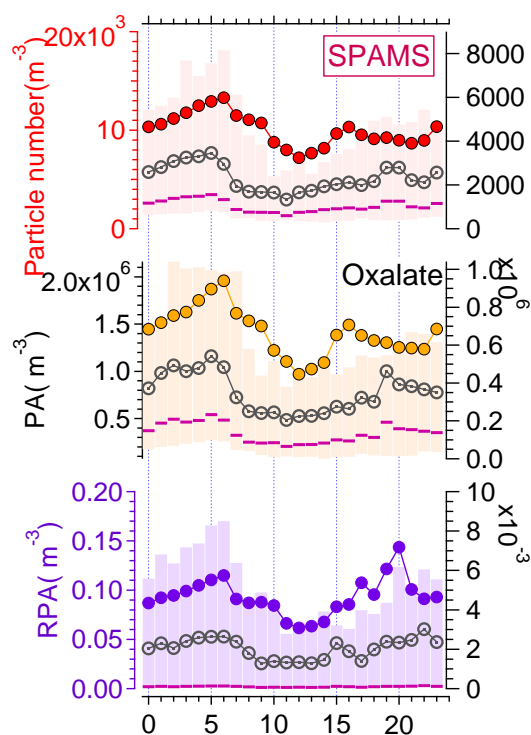


Figure S6 Diurnal variation of the particle number, peak area and relative peak area of oxalate measured by SPAMS (box represents the 25th and 75th percentiles of the data, horizontal line represents the median, and the solid round marker for the mean of the data; open circle also represents the median, but use the right axis for a better view).

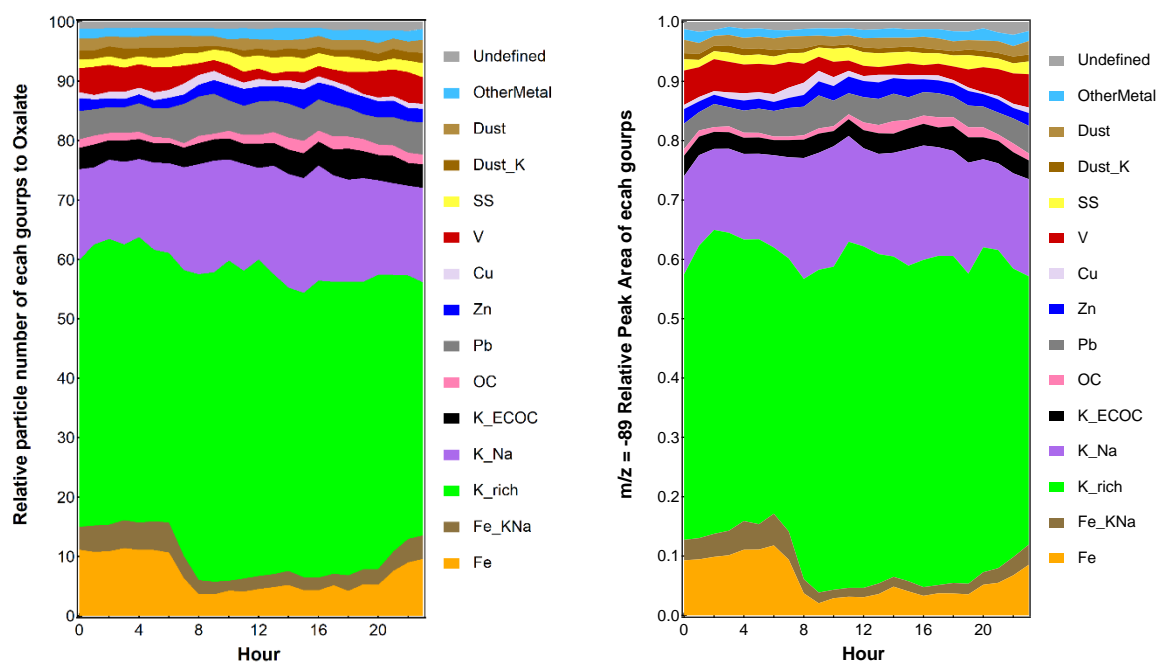


Figure S7 Relative contributions of oxalate intensity from each group to the total oxalate particle by a) peak area and b) relative peak area of m/z -89.

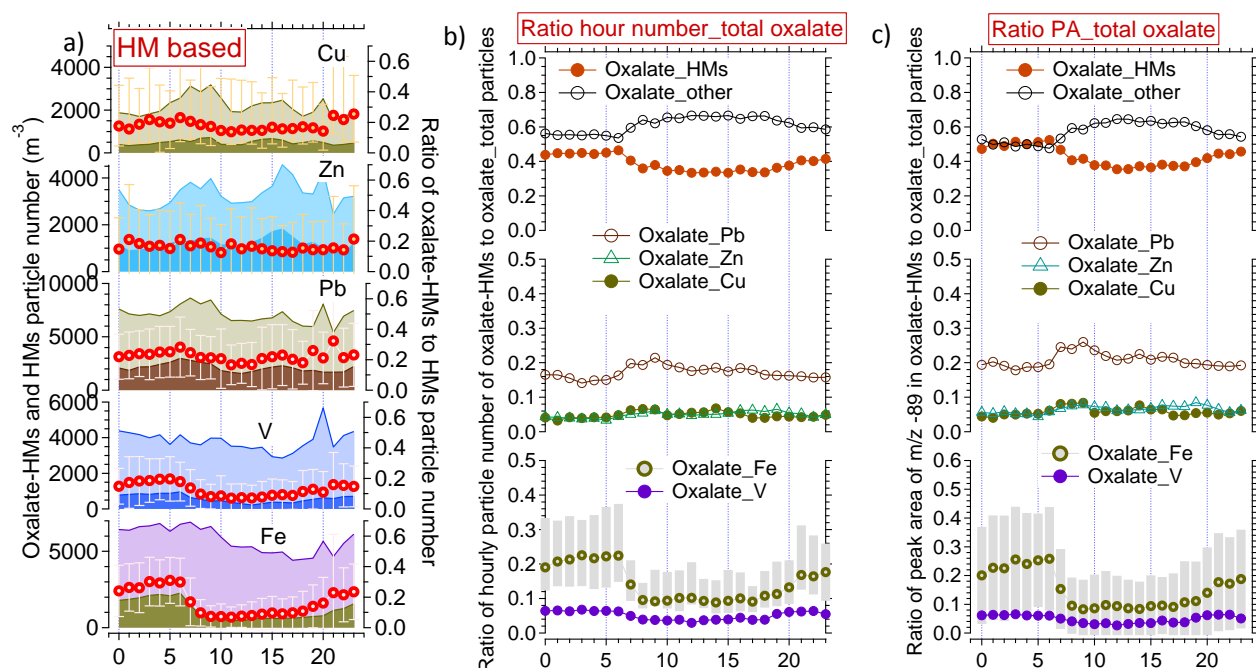


Figure S8 Diurnal variation of a) particle numbers of HMs and oxalate-HMs and the ratio of oxalate-HM to each metal, b) the ratio of oxalate-HM particle number to total oxalate and c) oxalate-HM peak area to total oxalate (a, Light and dark colors indicate the particle number of HMs and oxalate-HM particles respectively, the open circles indicate the ratio between oxalate-HM and HM particle numbers, error bars represent $1/4 \times$ standard deviation of the ratios; b and c, oxalate_other stands for oxalate particles without these five HMs, the standard deviation of the ratio of oxalate_Fe to oxalate and HMs was marked as box in the bottom panel)

The diurnal variation of these five heavy metals and the oxalate-HM particles is investigated in this work and shown in **Figure S8**. The particle number concentration ratio of oxalate-HM to HM (**Figure S8a**, circles, right axis) reveals a diurnal trend with a clear daytime minimum for oxalate-V/V and oxalate-Fe/Fe, and a less prominent daytime minimum for other HMs. This might be due to less oxalate in the daytime. Thus, we normalized the data by the total oxalate concentration as shown in **Figure S8b** and **S8c**. When we compare the particle number concentration ratio of oxalate-HM to total oxalate for each HM, the ratio of oxalate-Fe/oxalate clearly shows a significant morning decrease using particle number concentration (**Figure S8b**), and peak area (**Figure S8c**). For the other metals, only oxalate-V/oxalate shows a slight daytime decrease. These findings suggest Fe is the dominant metal that controls the degradation of oxalate in the early morning.

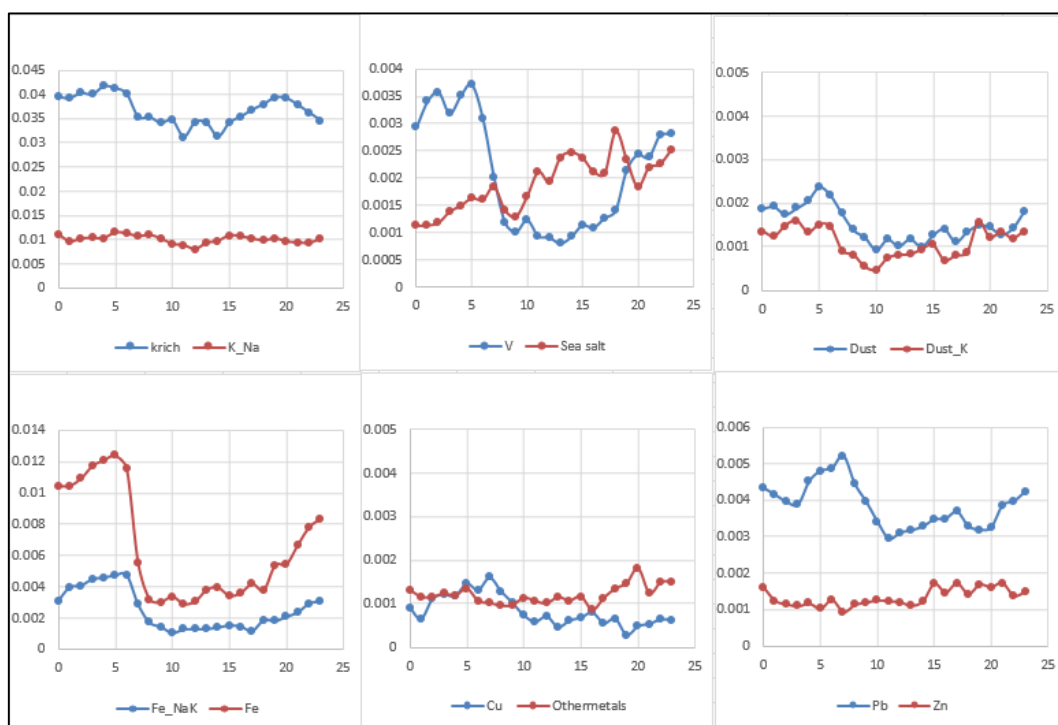


Figure S9 Average diurnal variations of the oxalate particle number from the classified groups to total mass particle number.

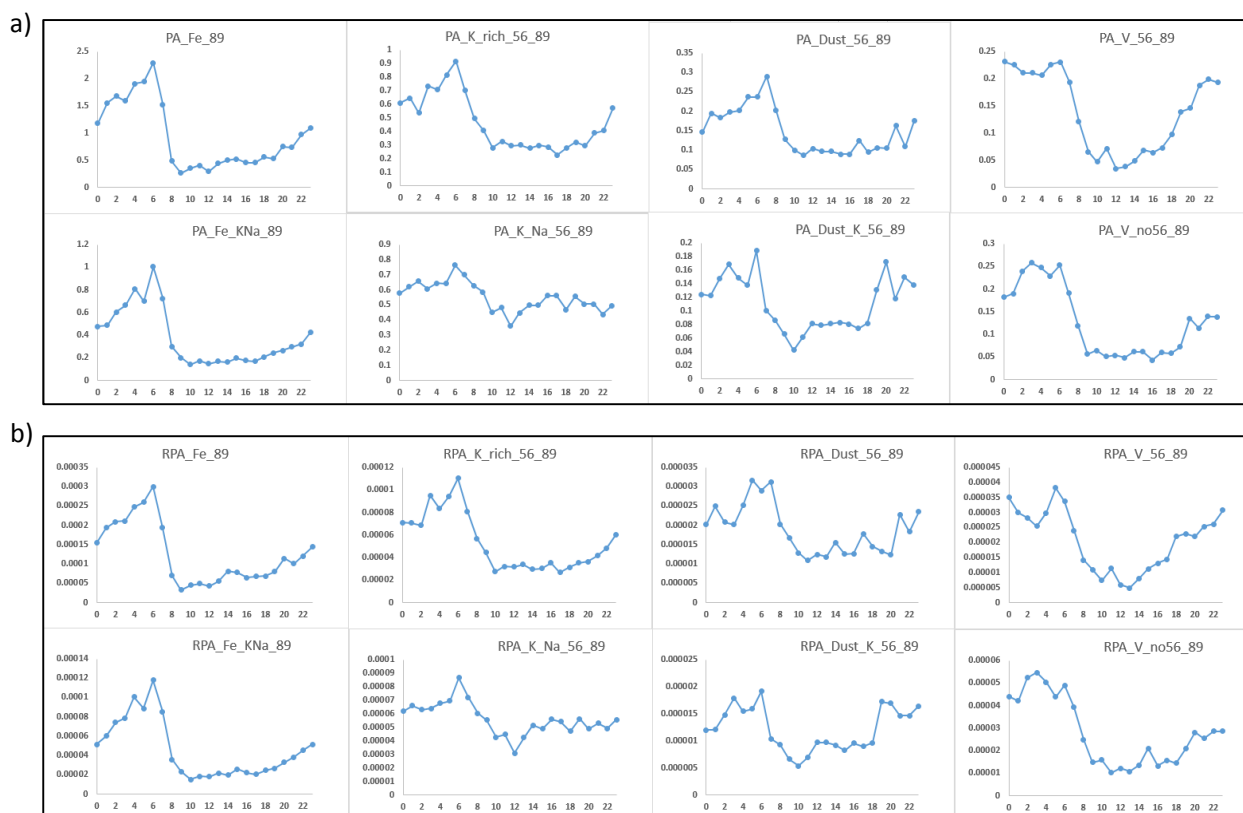


Figure S10 Diurnal variations of oxalate intensity in different Fe-containing oxalate particles by a) the peak area and b) relative peak area of m/z -89.

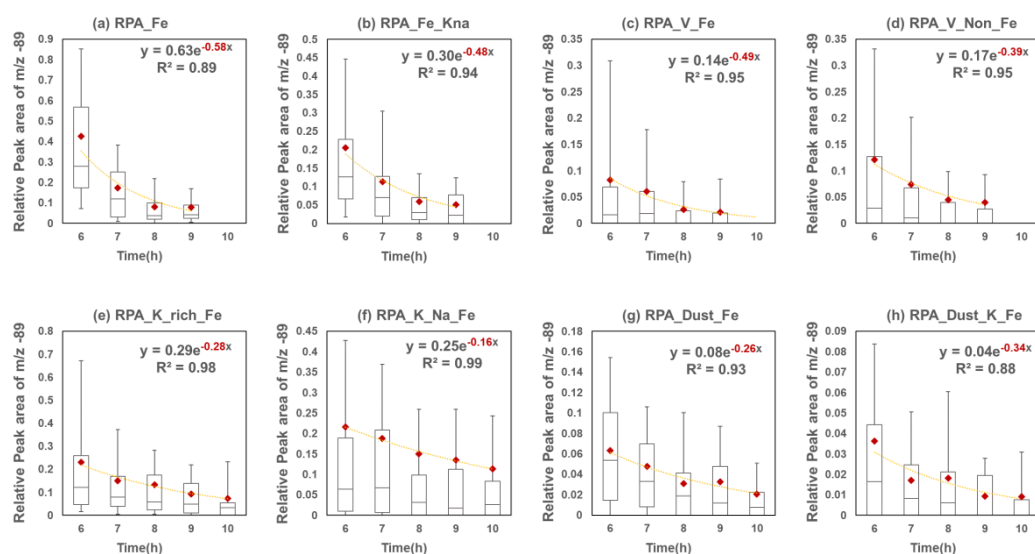


Figure S11 The average decay of oxalate intensity between 6-10 am from the oxalate-Fe complexes per the Art-2a particle classification. (Plotted by particle relative peak area of m/z -89 and the number in red indicates the fitted decay rate based on exponential curve; Box and error bars represent the 10th, 25th, 50th, 75th and 90th percentiles, respectively, and the red diamond represents the mean).

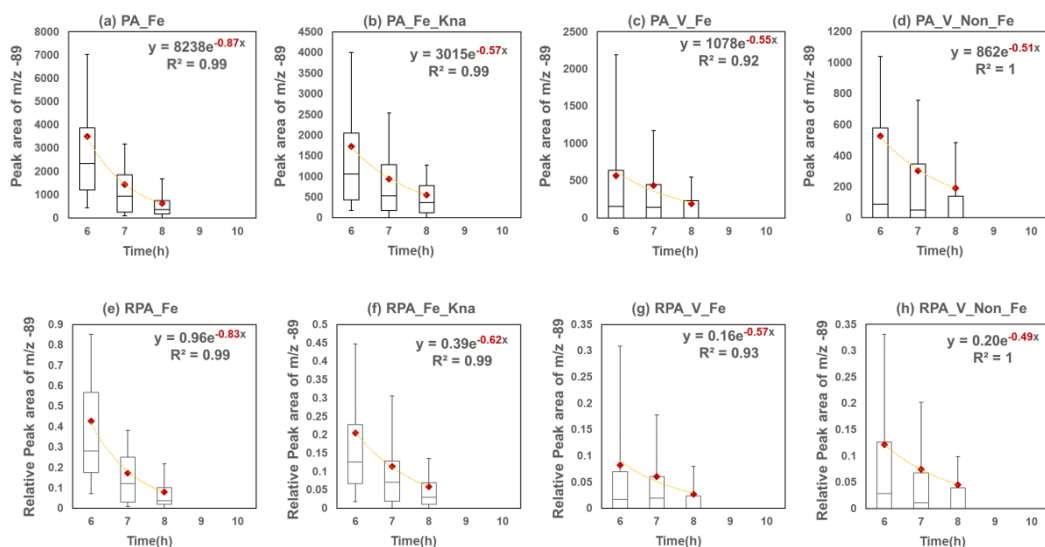


Figure S12 The average decay of oxalate intensity for the first three hours from the oxalate-Fe complexes per the Art-2a particle classification. (Plotted by particle peak area and relative peak area of m/z -89 and the number in red indicates the fitted decay rate based on exponential curve; Box and error bars represent the 10th, 25th, 50th, 75th and 90th percentiles, respectively, and the red diamond represents the mean).

S5 Temporal variations of oxalate_Fe complexes (Figure S13-S14)

Figure S13 shows the time series of the relative particle number (to mass particles) of oxalate, Fe and oxalate-Fe complex containing particles, together with that of meteorological parameters and percent contributions of individual oxalate particle groups. As illustrated in Figure S5, the presence of oxalate_Fe complexes was influenced by several factors, including the abundance of iron and oxalate and the meteorological conditions. Generally, variations in oxalate_Fe particle number fraction tracked with that of iron (e.g. Figure S5c, blue box), while at other times that of the oxalate particle number fraction (e.g. Figure S5c, red and orange boxes).

The meteorological parameters may also play an important role. As shown in Figure S5a, whenever the solar irradiation was low, it was often accompanied by precipitation and high humidity, which is favorable for oxalate-Fe complex formation in the particle aqueous layer, and slower photolytic degradation due to reduced solar irradiation. In particular, there were several fog events from February 4 to 6, and much higher contributions of oxalate_Fe complexes were observed. We will present case studies of special events in a future manuscript.

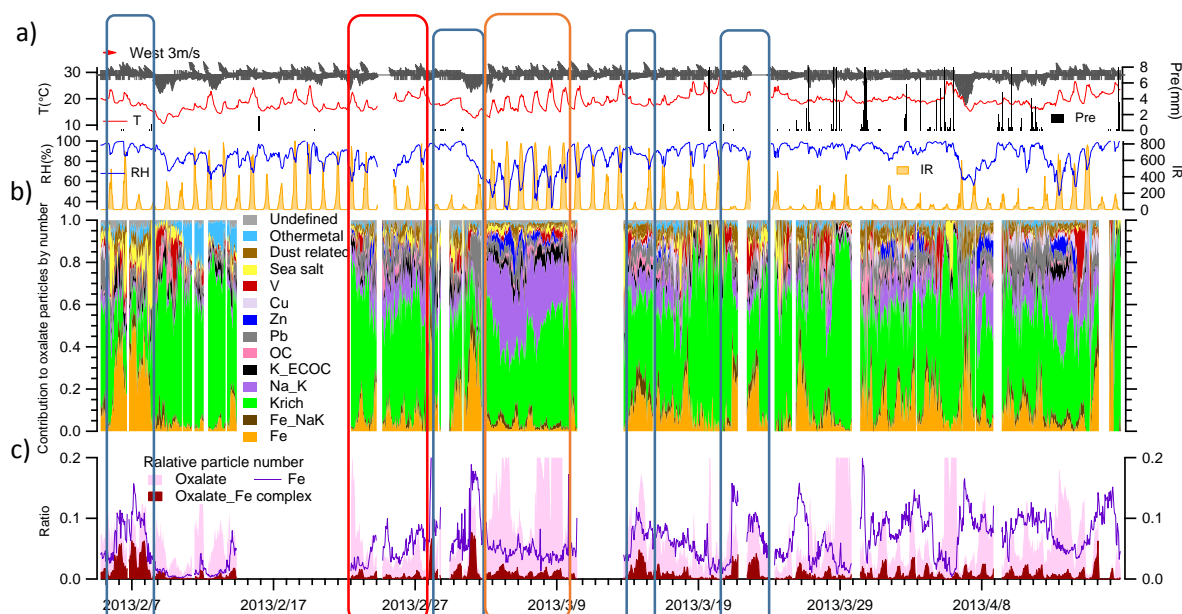


Figure S13 Time series of a) meteorological parameters, b) the contribution of each group to the total oxalate, by particle number and c) the relative particle number (to mass particles) of oxalate, Fe and oxalate-Fe complex containing particles. Panels a) and b) reproduce those in Figure 2.

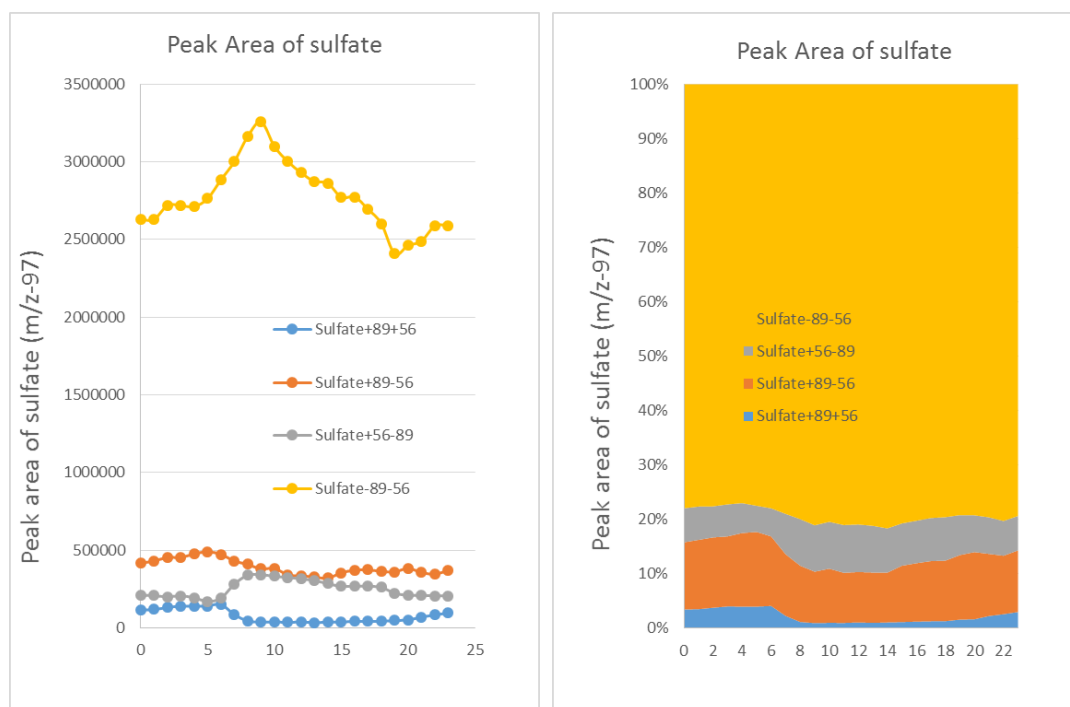


Figure S14 Diurnal variation of m/z -97 peak area for four separate sulfate groups.

S6 Discussion on minimizing the uncertainty of semi-quantification analysis by SPAMS

As noted in Section 3.5, matrix effects present a major difficulty that impairs the accuracy and precision of SPAMS using laser ablation. As a result, most of this study is based on statistics of the campaign averaged data set, and we track the oxalate and sulfate trends by particle number, PA and RPA to give more confidence that the observed phenomena are real. For all figures, we showed the particle number and PA information in the manuscript and the RPA information in the supporting information; thus readers can reference all data routes. Furthermore, we compared the SPAMS measurements over the averaged diurnal period with the MARGA bulk ion concentrations. Lastly, we performed inter- and intra-particle group comparisons to figure out the dominate source that drove the morning decay of oxalate and to estimate the formation of sulfate.

However, uncertainties may still exist in the sulfate formation calculation by SPAMS. From our previous study, for higher abundance species like sulfate and nitrate, we recommend to use RPA, while for lower abundance species like oxalate, we recommend to use PA.¹⁹ However, deriving sulfate formation in the presence of oxalate requires careful consideration. Sulfate is the dominant ion and presence of other ions will decrease its RPA even though the sulfate PA is increasing. As shown in figure S15a, the RPA of sulfate without oxalate and Fe (Sulfate-89-56, marked with blue) showed the highest individual RPA, while this type of sulfate particle showed the lowest PA (figure 6b). It is worth noting that both metrics yielded similar diurnal variations. The individual sulfate intensity of sulfate+56-89 particles showed an increase when the decomposition of oxalate-Fe occurred, but the RPA increase was relatively low (x1.2) compared with the PA (x1.6). No matter if the matrix effect existed in the sulfate with oxalate particles, the factor increase of 1.6 or 1.2 is based on the same type of particles, which minimizes the matrix effect. Nevertheless, the true uncertainty associated with the semi-quantitative analysis using the laser ablation instrument remains unresolved and needs further investigation.

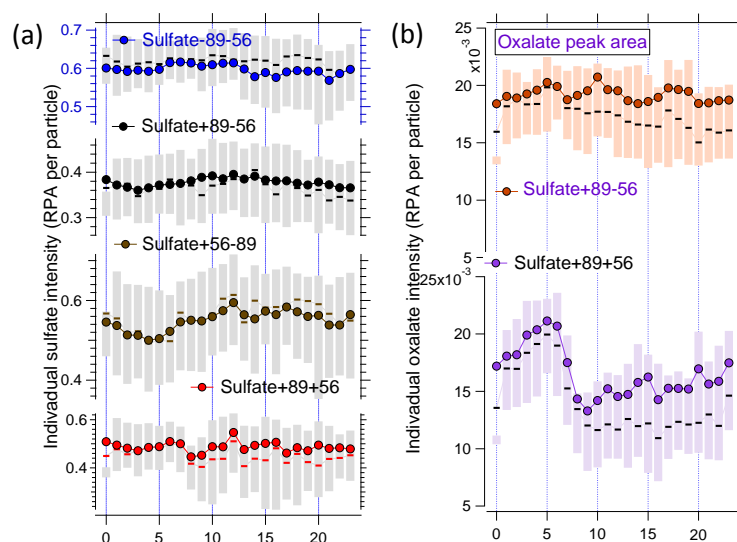


Figure S15 (a) Diurnal variation of the individual sulfate intensity and (b) oxalate intensity in two sulfate particle groups, including sulfate particles with both oxalate and iron (sulfate+89+56), with only oxalate (sulfate+89-56). (Box and line represent the 25th and 75th percentiles and median of RPA, respectively, and the open circle represents the mean)

References:

1. Li, L.; Huang, Z. X.; Dong, J. G.; Li, M.; Gao, W.; Nian, H. Q.; Fu, Z.; Zhang, G. H.; Bi, X. H.; Cheng, P.; Zhou, Z., Real time bipolar time-of-flight mass spectrometer for analyzing single aerosol particles. *Int. J. Mass spectrom.* **2011**, *303*, (2-3), 118-124.
2. Neubauer, K. R.; Johnston, M. V.; Wexler, A. S., Humidity effects on the mass spectra of single aerosol particles. *Atmos. Environ.* **1998**, *32*, (14-15), 2521-2529.
3. Zelenyuk, A.; Imre, D.; Cuadra-Rodriguez, L. A., Evaporation of water from particles in the aerodynamic lens inlet: An experimental study. *Anal. Chem.* **2006**, *78*, (19), 6942-6947.
4. Allen, J. O., Software Toolkit to Analyze Single-Particle Mass Spectral Data. **2001**.
5. Martell, A. E.; Smith, R. M., *Critical Stability Constants. Volume 3, Other organic ligands*. Springer: 1977.
6. Lide, D. R., *CRC Handbook of Chemistry and Physics, 75th*. CRC Press: Boston, 1994.
7. Moffet, R. C.; Desyaterik, Y.; Hopkins, R. J.; Tivanski, A. V.; Gilles, M. K.; Wang, Y.; Shutthanandan, V.; Molina, L. T.; Abraham, R. G.; Johnson, K. S., Characterization of aerosols containing Zn, Pb, and Cl from an industrial region of Mexico City. *Environ. Sci. Technol.* **2008**, *42*, (19), 7091-7097.
8. Hu, C. W.; Chao, M. R.; Wu, K. Y.; Chang-Chien, G. P.; Lee, W. J.; Chang, L. W.; Lee, W. S., Characterization of multiple airborne particulate metals in the surroundings of a municipal waste incinerator in Taiwan. *Atmos. Environ.* **2003**, *37*, (20), 2845-2852.
9. Ondov, J. M.; Wexler, A. S., Where do particulate toxins reside? An improved paradigm for the structure and dynamics of the urban mid-Atlantic aerosol. *Environ. Sci. Technol.* **1998**, *32*, (17), 2547-2555.
10. Jiun-Hong, T.; Kuo-Hsiung, L.; Chihyu, C.; Jian-Yuan, D.; Ching-Guan, C.; Hung-Lung, C., Chemical constituents in particulate emissions from an integrated iron and steel facility. *J. Hazard. Mater.* **2007**, *147*, (1-2), 111-119.
11. Moffet, R.; Foy, B. d.; Molina, L. a.; Molina, M.; Prather, K., Measurement of ambient aerosols in northern Mexico City by single particle mass spectrometry. *Atmos. Chem. Phys.* **2008**, *8*, (16), 4499-4516.
12. Ault, A. P.; Gaston, C. J.; Wang, Y.; Dominguez, G.; Thiemens, M. H.; Prather, K. A., Characterization of the single particle mixing state of individual ship plume events measured at the port of Los Angeles. *Environ. Sci. Technol.* **2010**, *44*, (6), 1954-1961.

13. Ault, A. P.; Moore, M. J.; Furutani, H.; Prather, K. A., Impact of Emissions from the Los Angeles Port Region on San Diego Air Quality during Regional Transport Events. *Environ. Sci. Technol.* **2009**, *43*, (10), 3500-3506.
14. Agrawal, H.; Welch, W. A.; Miller, J. W.; Cocker, D. R., Emission measurements from a crude oil tanker at sea. *Environ. Sci. Technol.* **2008**, *42*, (19), 7098-7103.
15. Fernández, A. J.; Ternero, M.; Barragán, F. J.; Jiménez, J. C., An approach to characterization of sources of urban airborne particles through heavy metal speciation. *Chemosphere-Global Change Science* **2000**, *2*, (2), 123-136.
16. Chang, M. B.; Huang, C. K.; Wu, H. T.; Lin, J. J.; Chang, S. H., Characteristics of heavy metals on particles with different sizes from municipal solid waste incineration. *J. Hazard. Mater.* **2000**, *79*, (3), 229-239.
17. Walsh, D. C.; Chillrud, S. N.; Simpson, H. J.; Bopp, R. F., Refuse incinerator particulate emissions and combustion residues for New York City during the 20th century. *Environ. Sci. Technol.* **2001**, *35*, (12), 2441-2447.
18. Zhuang, H.; Chan, C. K.; Fang, M.; Wexler, A. S., Formation of nitrate and non-sea-salt sulfate on coarse particles. *Atmos. Environ.* **1999**, *33*, (26), 4223-4233.
19. Zhou, Y.; Huang, X. H. H.; Griffith, S. M.; Li, M.; Li, L.; Zhou, Z.; Meng, J.; Chan, C. K.; Louie, P. K. K.; Yu, J. Z., A field measurement based scaling approach for quantification of major ions, organic carbon, and elemental carbon using a single particle aerosol mass spectrometer. *Atmos. Environ.* **2016**, *143*, 300-312.